Measurement of the neutron-induced fission cross section of ^{230}Th at the CERN n_TOF facility

V. Michalopoulou,[1,2,*] A. Stamatopoulos,[1] M. Diakaki,[1] A. Tsinganis,[2,3] R. Vlastou,[1] M. Kokkoris,[1] N. Patronis,[4] Z. Eleme,[4] D. Macina,[2] L. Tassan-Got,[2,1,5] N. Colonna,[6] E. Chiaveri,[2] A. Ventura,[7] P. Schillebeeckx,[3] J. Heyse,[3] G. Sibbens,[3] G. Alaerts,[3] A. Borella,[8] A. Moens,[3] D. Vanleeuw,[3] O. Aberle,[9] V. Alcayne,[10] S. Amaducci,[11,12] J. Andrzejewski,[13] L. Audouin,[5] V. Babiano-Suarez,[14] M. Bacak,[2,15,16] M. Barbagallo,[2,17] S. Bennett,[18] E. Berthoumieux,[16] J. Billowes,[18] D. Bosnar,[19] A. Brown,[20] M. Busso,[21,22] M. Caamaño,[23] L. Caballero,[14] F. Calviño,[24] M. Calviani,[2] D. Cano-Ott,[10] A. Casanovas,[24] F. Cerutti,[2] G. Cortés,[24] M. A. Cortés-Giraldo,[25] L. Cosentino,[11] S. Cristallo,[21,26] L. A. Damone,[17,27] P. J. Davies,[18] M. Dietz,[28] C. Domingo-Pardo,[14] R. Dressler,[29] Q. Ducasse,[30] E. Dupont,[16] I. Durán,[23] B. Fernández-Domínguez,[23] A. Ferrari,[2] P. Finocchiaro,[11] V. Furman,[31] K. Göbel,[32] R. Garg,[28] A. Gawlik-Ramięga,[13] S. Gilardoni,[2] I. F. Gonçalves,[33] E. González-Romero,[10] C. Guerrero,[25] F. Gunsing,[16] H. Harada,[34] S. Heinitz,[29] D. G. Jenkins,[20] A. Junghans,[35] F. Käppeler,[36,†] Y. Kadi,[2] A. Kimura,[34] I. Knapová,[37] Y. Kopatch,[31] M. Krtička,[37] D. Kurtulgil,[32] I. Ladarescu,[14] C. Lederer-Woods,[28] H. Leeb,[15] J. Lerendegui-Marco,[25] S. J. Lonsdale,[28] A. Manna,[7,38] T. Martínez,[10] A. Masi,[2] C. Massimi,[7,38] P. Mastinu,[39] M. Mastromarco,[2] E. A. Maugeri,[29] A. Mazzone,[17,40] E. Mendoza,[10] A. Mengoni,[41] P. M. Milazzo,[42] F. Mingrone,[2] J. Moreno-Soto,[16] A. Musumarra,[11,12] A. Negret,[43] R. Nolte,[30] F. Ogállar,[44] A. Oprea,[43] A. Pavlik,[45] J. Perkowski,[13] C. Petrone,[43] L. Piersanti,[21,26] E. Pirovano,[30] I. Porras,[44] J. Praena,[44] J. M. Quesada,[25] D. Ramos-Doval,[5] T. Rauscher,[46,47] R. Reifarth,[32] D. Rochman,[29] Y. Romanets,[33] C. Rubbia,[2] M. Sabaté-Gilarte,[25,2] A. Saxena,[48] D. Schumann,[29] A. Sekhar,[18] A. G. Smith,[18] N. V. Sosnin,[18] P. Sprung,[29] G. Tagliente,[17] J. L. Tain,[14] A. Tarifeño-Saldivia,[24] Th. Thomas,[32] P. Torres-Sánchez,[44] J. Ulrich,[29] S. Urlass,[35,2] S. Valenta,[37] G. Vannini,[7,38] V. Variale,[17] P. Vaz,[33] D. Vescovi,[21] V. Vlachoudis,[2] A. Wallner,[49] P. J. Woods,[28] T. Wright,[18] and P. Žugec[19]
(n_TOF Collaboration)[‡]

[1]*Department of Physics, National Technical University of Athens, Zografou Campus, Athens, Greece*
[2]*European Organisation for Nuclear Research (CERN), Geneva, Switzerland*
[3]*Joint Research Centre (JRC), European Commission, Geel, Belgium*
[4]*Department of Physics, University of Ioannina, University Campus, Ioannina, Greece*
[5]*Institut de Physique Nucléaire, CNRS-IN2P3, Université Paris-Sud, Université Paris-Saclay, F-91406 Orsay Cedex, France*
[6]*Istituto Nazionale di Fisica Nucleare, Bari, Italy*
[7]*Istituto Nazionale di Fisica Nucleare, Sezione di Bologna, Bologna, Italy*
[8]*Belgian Nuclear Research Centre (SCK CEN), Boeretang 200, 2400 Mol, Belgium*
[9]*European Organization for Nuclear Research (CERN), Geneva, Switzerland*
[10]*Centro de Investigaciones Energéticas Medioambientales y Tecnológicas (CIEMAT), Madrid, Spain*
[11]*INFN Laboratori Nazionali del Sud, Catania, Italy*
[12]*Dipartimento di Fisica e Astronomia, Università di Catania, Catania, Italy*
[13]*University of Lodz, Lodz, Poland*
[14]*Instituto de Física Corpuscular, CSIC - Universidad de Valencia, Valencia, Spain*
[15]*TU Wien, Atominstitut, Stadionallee 2, 1020 Wien, Austria*
[16]*CEA Irfu, Université Paris-Saclay, F-91191 Gif-sur-Yvette, France*
[17]*Istituto Nazionale di Fisica Nucleare, Sezione di Bari, Bari, Italy*
[18]*University of Manchester, Manchester, United Kingdom*
[19]*Department of Physics, Faculty of Science, University of Zagreb, Zagreb, Croatia*
[20]*University of York, York, United Kingdom*
[21]*Istituto Nazionale di Fisica Nucleare, Sezione di Perugia, Perugia, Italy*
[22]*Dipartimento di Fisica e Geologia, Università di Perugia, Perugia, Italy*
[23]*University of Santiago de Compostela, Santiago de Compostela, Spain*
[24]*Universitat Politècnica de Catalunya, Barcelona, Spain*
[25]*Universidad de Sevilla, Seville, Spain*
[26]*Istituto Nazionale di Astrofisica - Osservatorio Astronomico d'Abruzzo, Teramo, Italy*
[27]*Dipartimento Interateneo di Fisica, Università degli Studi di Bari, Bari, Italy*
[28]*School of Physics and Astronomy, University of Edinburgh, Edinburgh, United Kingdom*

[*]veatriki.michalopoulou@cern.ch
[†]Deceased.
[‡]www.cern.ch/ntof

[29]*Paul Scherrer Institut (PSI), Villigen, Switzerland*
[30]*Physikalisch-Technische Bundesanstalt (PTB), Bundesallee 100, 38116 Braunschweig, Germany*
[31]*Affiliated with an institute covered by a cooperation agreement with CERN*
[32]*Goethe University Frankfurt, Frankfurt, Germany*
[33]*Instituto Superior Técnico, Lisbon, Portugal*
[34]*Japan Atomic Energy Agency (JAEA), Tokai-Mura, Japan*
[35]*Helmholtz-Zentrum Dresden-Rossendorf, Dresden, Germany*
[36]*Karlsruhe Institute of Technology, Campus North, IKP, 76021 Karlsruhe, Germany*
[37]*Charles University, Prague, Czech Republic*
[38]*Dipartimento di Fisica e Astronomia, Università di Bologna, Bologna, Italy*
[39]*Istituto Nazionale di Fisica Nucleare, Sezione di Legnaro, Legnaro, Italy*
[40]*Consiglio Nazionale delle Ricerche, Bari, Italy*
[41]*Agenzia Nazionale per le Nuove Tecnologie (ENEA), Bologna, Italy*
[42]*Istituto Nazionale di Fisica Nucleare, Sezione di Trieste, Trieste, Italy*
[43]*Horia Hulubei National Institute of Physics and Nuclear Engineering, Bucharest-Magurele, Romania*
[44]*University of Granada, Granada, Spain*
[45]*Faculty of Physics, University of Vienna, Vienna, Austria*
[46]*Department of Physics, University of Basel, Basel, Switzerland*
[47]*Centre for Astrophysics Research, University of Hertfordshire, Hatfield, United Kingdom*
[48]*Bhabha Atomic Research Centre (BARC), Mumbai, India*
[49]*Australian National University, Canberra, Australia*

(Received 17 March 2023; accepted 26 May 2023; published 26 July 2023; corrected 1 August 2023)

The neutron-induced fission cross section of ^{230}Th has been measured at the neutron time-of-flight facility n_TOF located at CERN. The experiment was performed at the experimental area EAR-1 with a neutron flight path of 185 m, using Micromegas detectors for the detection of the fission fragments. The ^{230}Th(n, f) cross section was determined relative to the ^{235}U(n, f) one, covering the energy range from the fission threshold up to 400 MeV. The results from the present work are compared with existing cross-section datasets and the observed discrepancies are discussed and analyzed. Finally, using the code EMPIRE 3.2.3 a theoretical study, based on the statistical model, was performed leading to a satisfactory reproduction of the experimental results with the proper tuning of the respective parameters, while for incident neutron energy beyond 200 MeV the fission of ^{230}Th was described by Monte Carlo simulations.

DOI: 10.1103/PhysRevC.108.014616

I. INTRODUCTION

Accurate neutron-induced fission cross-section data on actinides play an important role in the research and design of advanced nuclear systems. More specifically, the study of the isotopes present in the thorium cycle, which is proposed as an alternative to the conventional uranium-plutonium one, can assist in the development of the relevant nuclear systems aiming at making the production of energy safer, sustainable, economic, and proliferation resistant [1].

In particular, ^{230}Th is produced in the thorium cycle from the α decay of ^{234}U, and has almost two times higher neutron-induced fission cross section than ^{232}Th in the fast energy region, which contributes to the neutron balance, assisting this way in the breeding of the fissile isotope ^{233}U.

Additionally, the study of neutron-induced fission cross sections plays a key role in the understanding of the fission process and the parameters of fission barriers. In thorium nuclides, narrow resonances and fine structures have been observed in the threshold region of the fission cross section, known as the "thorium anomaly." Specifically, previous measurements of the ^{230}Th(n, f) cross section revealed a large and well isolated resonance near 700 keV with additional fine structures near the fission threshold. Various theoretical investigations attempting to explain the ^{230}Th resonance exist in the literature, in the framework of the double- [2–4] and triple-humped fission barriers [5–11]. These structures suggest the existence of a third well in the fission barrier [12], which allows the existence of Class-III vibrational states that could explain the existing structures near the fission threshold.

Despite the above-mentioned fields of interest, only a few experimental datasets exist in the literature for the neutron-induced fission cross section of ^{230}Th, mainly due to the challenge in the target preparation of this natural but also very rare isotope. The existing datasets exhibit large uncertainties (more than 5% for the majority of the data points) and discrepancies among them, while they cover only the energy range from the fission threshold up to 25 MeV, as presented in Fig. 1.

The most recent measurements of Goldblum *et al.* [13] and Petit *et al.* [14] are based on the indirect determination of the ^{230}Th neutron-induced fission cross section via the surrogate ^{232}Th$(^3$He$, \alpha)$ reaction. The measurements of Meadows [15,16], Boldeman and Walsh [11], James *et al.* [3], and Kazarinova *et al.* [17] were performed with quasi-monoenergetic neutron beams, produced via charged particle reactions. The measurement of Blons *et al.* [6] was performed with the time-of-flight technique, while the data of Muir and

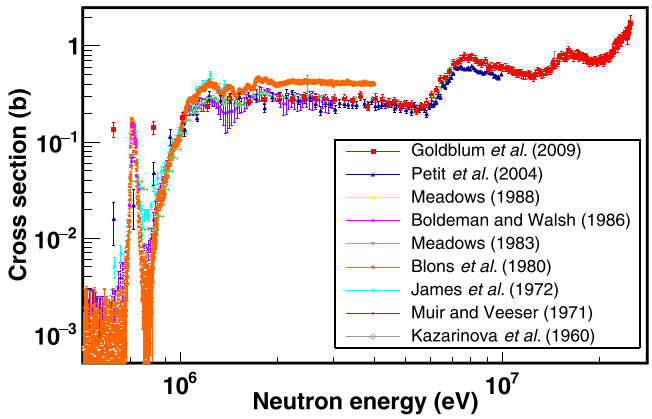

FIG. 1. Experimental data for the neutron-induced fission cross section of ^{230}Th available in the literature. The data present discrepancies and cover the energy range from the fission threshold up to 25 MeV. The measurements of the present work can assist in resolving the discrepancies and provide data at higher energies.

Veeser [18] were obtained using neutrons from an underground nuclear explosion. The cross-section data points of Blons *et al.* and James *et al.* exhibit systematically higher cross-section values, at all neutron energies, compared to the other datasets in literature. In these two datasets the fission yield per neutron is converted to fission cross section by normalizing to the value 0.37 b at 1.4 MeV (that has not been published), after private communication of the authors with Evans and Jones [3,6].

The discrepancies between the experimental cross-section data in the literature, along with the uncertainties that they exhibit, are reflected in the large deviations between the latest versions of nuclear evaluations over the whole energy region, as presented in Fig. 2. These differences show a demand for additional high-accuracy experimental data, while higher energy data would be also interesting to extend the energy region of the current evaluations.

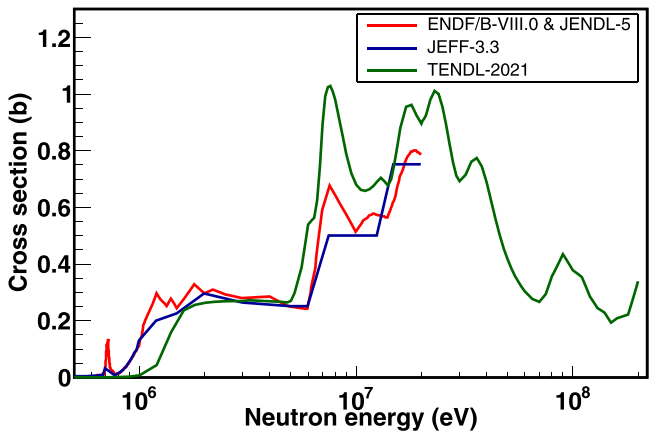

FIG. 2. Evaluated cross-section data for the ^{230}Th(n, f) reaction from ENDF/B-VIII.0 [19] which adopts the JENDL-5.0 library [20] (red), JEFF-3.3 [21] (blue), and TENDL-2021 [22] (green). Large differences are observed between the evaluation libraries. The data of this work can help in improving the evaluations.

For this purpose, the measurement of the neutron-induced fission cross section of ^{230}Th was performed at the neutron time-of-flight facility n_TOF, located at the European Organization for Nuclear Research (CERN). The experimental area EAR-1 with the long 185 m neutron flight path was used to acquire high neutron energy resolution data from the fission threshold up to 400 MeV, combined with complementary measurements at the experimental area EAR-2 with a shorter neutron flight path of about 19 m. The experimental setup, as well as the details of the analysis procedure, will be presented, along with theoretical calculations.

II. EXPERIMENTAL SETUP

The cross section up to 400 MeV was determined by the experiment carried out at the experimental area EAR-1 of the n_TOF facility [23,24], located at CERN. An additional measurement with the same detection setup was performed at the experimental area EAR-2 [25], specifically for the estimation of the contaminants in the ^{230}Th samples. The neutron beam was produced via spallation of a lead target by a pulsed beam of 20 GeV/c protons providing a white neutron spectrum ranging from the thermal region up to ≈1 GeV. Two pulse modes are provided by the CERN Proton Synchrotron (PS): the dedicated ones corresponding to the nominal intensity of the proton bunch [(7–8) × 10^{12}] and the parasitic ones corresponding to a lower intensity (3 × 10^{12}).

The neutrons travel a horizontal flight-path of 185 m before they reach the experimental area EAR-1, rendering high neutron energy resolution measurements possible with high instantaneous neutron fluence per proton pulse. A smaller vertical flight path of ≈19 m is available at the experimental area EAR-2, which provides approximately an order of magnitude higher neutron fluence per proton pulse, making it ideal for measurements of very small cross sections, small sample masses and radioactive samples.

A. Actinide samples

Seven high purity ^{230}Th samples were produced and characterised at the target preparation laboratory of JRC-Geel [26]. The base material was analysed for its isotopic composition by inductively coupled plasma mass spectrometry [27] and for the amount of plutonium by isotope dilution mass spectrometry [28] at the nuclear chemistry and nuclear mass spectrometry laboratories at JRC-Geel. This resulted in the mass ratios ^{230}Th/Th = 0.915 750(34), ^{232}Th/Th = 0.084 250(34), and Pu/Th = 0.000 494 2(20). The samples were prepared by molecular plating in isopropanol on a 0.025 mm thick aluminum foil [26]. The foil was stretched and glued on a 2 mm thick aluminum ring with an inner and outer diameter of 100 and 110 mm, respectively. A mask with an inner diameter of 80.00(2) mm was placed on top of the aluminum foil defining the effective area of the ^{230}Th deposit.

The activities of the ^{230}Th samples were determined by α-particle counting at a defined solid-angle. The samples were positioned parallel to and coaxial with a Si surface barrier detector at a well-defined distance. The relative solid angle between the source and the detector was determined by the

TABLE I. Mass, activity, and number of atoms of the ^{230}Th samples. The quoted uncertainty is the combined uncertainty due to the counting statistics, a 0.12% random component explained in the text and the uncertainty due to the correction for the ^{226}Ra contribution. For the total uncertainty the latter contribution has to be combined with a common component of 0.65%. The target ID indicates the position of the target in the chamber with respect to the neutron beam.

Target ID	Reference number	Mass (mg)	Activity (MBq)	Number of nuclei ($\times 10^{19}$)
^{230}Th #3	TP2017-06-19	4.546(8)	3.468(6)	1.190(21)
^{230}Th #4	TP2017-06-21	4.053(13)	3.092(10)	1.061(34)
^{230}Th #5	TP2017-06-24	2.249(9)	1.716(7)	0.5889(24)
^{230}Th #6	TP2017-06-22	2.464(8)	1.880(6)	0.6541(21)
^{230}Th #7	TP2017-06-25	4.118(16)	3.142(12)	1.078(41)
^{230}Th #8	TP2017-06-20	4.848(13)	3.698(10)	1.269(34)
^{230}Th #9	TP2017-06-18	4.441(9)	3.388(7)	1.163(24)

distance, the sample size and the knife-edged aperture of a diaphragm placed just in from of the detector. The use of the diaphragm allows for a more accurate determination of the detection geometry, as its diameter is defined more accurately than the one of the detector's surface [29].

The results are summarized in Table I, with the decay constant $\lambda = 2.91 \times 10^{-13}$ s^{-1} [30] used for the estimation of the number of nuclei. To avoid contamination in the α-particle counter each sample was placed in a plexiglass container which was closed with a 2 μm thick mylar foil covered with a 50 nm thick aluminum layer. The transmission probability through this foil was verified by measurements with a ^{237}Np sample and resulted in $T_\alpha = 1.0000(26)$. The procedure described in Ref. [31] was applied to calculate the solid angle $\Omega = 8.23(4) \times 10^{-4}$ sr subtended by the sample and the diaphragm. The main contribution in the uncertainty of the solid angle originates from the distance between the sample placed in the plexiglass container and the diaphragm in front of the detector which was $d = 170.7(3)$ mm. The intrinsic detection efficiency of the α-particle detector $\epsilon_\alpha = 0.9988(38)$ was derived by measurements with ^{235}U certified reference samples [32]. The above-mentioned uncertainties resulted in a final uncertainty component of 0.65%. A random uncertainty component of 0.12% reflects problems with reproducibility of the measurement conditions. This uncertainty, which is larger than the uncertainty due to counting statistics, was evaluated by a series of measurements dedicated for an analysis of variance (ANOVA) procedure [33].

The ^{230}Th activity was derived from the integrated count rate corresponding to 1.0–4.9 MeV deposited α-particle energy. In this energy region there is a parasitic contribution from the decay of ^{226}Ra as daughter product of ^{230}Th, while the one due to the decay of ^{232}Th can be neglected. The contribution from the ^{226}Ra decay was determined by additional γ-ray spectroscopic measurements using a high-purity germanium (HPGe) detector. This detection system was calibrated by combining results of measurements with a ^{235}U reference sample with the same diameter and a set of certified radionuclide sources. The uncertainty of the ratio is dominated by the γ-ray emission probabilities for the decay of ^{230}Th which are about 8% [30]. The γ-ray detection system was also used to verify the total activity of the samples. The results are fully consistent with those derived from the α-particle counting within the aforementioned uncertainties.

High-purity ^{235}U and ^{238}U reference samples, with the same geometrical characteristics as the ^{230}Th samples, were produced and characterized at JRC-Geel. They were both prepared by molecular plating using diaphragms and support rings with the same characteristics as those for the ^{230}Th. The isotopic compositions of the base material for these samples were determined by thermal ionization mass spectrometry [34] at JRC-Geel. The ^{235}U sample, with an activity of 288.0(13) Bq, was placed upstream of the ^{230}Th samples with respect to the neutron beam, while the ^{238}U sample, with an activity of 179.5(9) Bq, was placed after the stack of the ^{230}Th targets (see Fig. 3). Additionally, a ^{10}B reference sample, with the same diameter as the Th ones, was produced with an e-beam evaporator [35]. This sample was placed at the top of the stack of samples with respect to the neutron beam (see Fig. 3). The intention was to use this sample to determine the energy distribution of the incident neutron beam at the low energy region. However, due to the impact of the fissile Pu

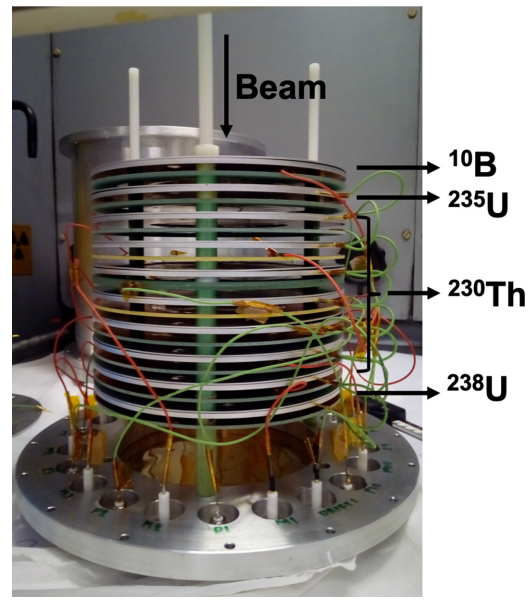

FIG. 3. A photograph of the stack of the Micromegas detectors and samples assembly used in the experiment. The seven ^{230}Th targets were placed between the reference targets.

isotopes present in the ^{230}Th samples an analysis of the data in this region could not be done (see Sec. III E).

B. Micromegas detectors

A setup based on MicroBulk Micromegas (Micro-Mesh Gaseous Structure) detectors [36–39] was used for the detection of the fission fragments. The Micromegas is a two-region gas detector divided by the micromesh (cathode electrode), which is a 5 μm thick Cu plate with holes of ≈35 μm in diameter at a distance of ≈50 μm from each other. The drift region is located between the drift electrode, which is the sample itself, and the micromesh, while the distance is chosen according to the requirements of each experiment (i.e., timing characteristics, pulse shape, particle energy deposition in the gas, etc.) and in this case it was set to 6 mm. The amplification region is located in the region between the micromesh and the anode, with a fixed distance between the two equal to 50 μm.

When an ionizing particle enters the drift region it creates electron-ion pairs, which drift towards the mesh due to the electric field in the region (≈ 1 kV/cm). The electrons enter the amplification region through the micromesh holes and they are multiplied through avalanches guided from the second, strong electric field (≈ 50 kV/cm). In this work, the induced signal was collected from the micromesh electrode.

Each sample was coupled to a separate Micromegas detector, while the whole sample-Micromegas assembly, as presented in Fig. 3, was placed in an aluminum chamber. The chamber was filled with a gas mixture of Ar:CF_4:isoC_4H_{10} (88:10:2), kept at room temperature and a constant pressure (≈ 1 atm).

C. Electronics and data acquisition

For the voltage supply, as well as the collection of the signals from the micromesh, individual current-sensitive preamplifier modules were implemented, constructed at INFN-Bari. The preamplifier output signals were fed to fast digitizers, in order to transform and record the corresponding waveforms.

III. DATA ANALYSIS

The data analysis aims at the identification of the fission pulses and the determination of their amplitude and time of arrival, which is eventually converted to the corresponding neutron energy. To achieve this, the raw data are initially analyzed with a pulse analysis (PSA) routine developed at n_TOF [40] and then processed to ensure the accurate recognition of the fission events. In addition, various corrections, such as the fraction of fission fragments rejected by the amplitude cut introduced in the analysis, the correction for pileup, etc., are applied to the data.

A. Raw data analysis

The raw data analysis begins with the accurate recognition of fission events, while rejecting α signals from the natural radioactivity of the samples, noise, and residuals from the γ-flash subtraction. Following the proper assessment, the amplitude of each signal is recorded, as well as its time of arrival, which is determined relative to the γ-flash peak.

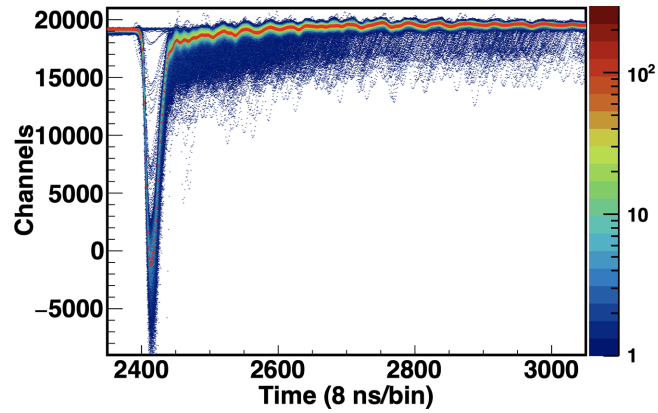

FIG. 4. γ-flash stack from various events. The average γ-flash shape and the subsequent baseline (red line) are estimated from the stack.

The γ-flash peak is the first peak present in the time spectra, originating from high energy deposition events in the detector (see Fig. 4), mainly from γ rays and other high-energy relativistic particles, which occur during the spallation process, as well as high-energy neutrons. After the γ-flash peak, an oscillatory baseline was recorded. In order to mitigate the γ-flash effects and accurately determine the amplitude and time of arrival of fission fragments induced from high energy neutrons, the methodology described in [41] was implemented.

The treatment of the γ-flash was based on the estimation of an average shape for the γ-flash peak and the subsequent baseline. In this scope, a stack of several γ-flash peaks was created, which originates from actual experimental data placed one on top of the other. The z axis of the stack represents by a color scale the counts that have been recorded in each bin in the stacked histogram. By applying a threshold value on the z axis the average γ-flash shape is estimated, while the fission fragment signals are discarded from the estimation of the average shape. In Fig. 4 the stack of the γ-flash peaks is shown, in which the first peak at all bunches was the γ-flash, while various other signals corresponding to fission fragments and α particles were present at later times-of-flight. The average γ-flash shape (red line) is also shown. The average γ-flash shape and the subsequent baseline were then subtracted from each single event, after normalizing to the amplitude of the γ-flash peak in the event.

For the identification of the fission pulses, the PSA was implemented. Pulses were recognized when their derivative crossed a certain threshold. Then, if any of the eliminating criteria were met, such as the limits of the pulse amplitude and the limits of the area-to-amplitude ratio, the pulse was recorded as a true event. The pulse recognition was followed by the estimation of the baseline, which is taken from the average γ-flash shape for higher neutron energies, while a constant baseline was assumed in the lower energy region, where the effects of the γ-flash are not present. Finally, the pulse reconstruction was achieved with the pulse shape fitting

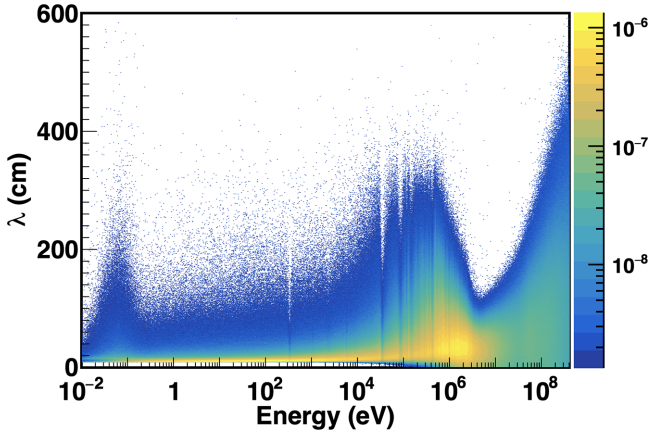

FIG. 5. Distribution of the moderation length λ as a function of the neutron energy.

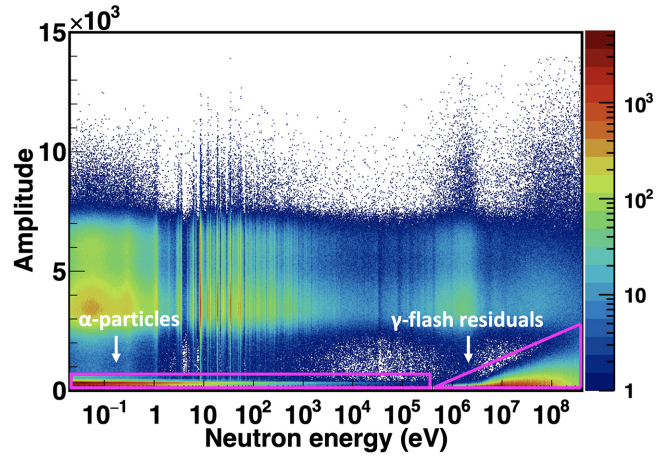

FIG. 6. Distribution of the amplitude of the signals for the ^{235}U sample as a function of the neutron energy. The α particles from the natural radioactivity of the target are present in the low energy region and the γ-flash residuals (increasing with energy) are present in the high energy region.

method. In order to do so, various experimental fission pulses were provided to the routine and the best fit was selected according to the minimum chi-square value. Additional information on the PSA procedure can be found in Ref. [40].

B. Flight path length

A very crucial step for the calculation of the ^{230}Th(n, f) cross section at each neutron energy was the conversion of the time-of-flight of the signals to the equivalent neutron energy, which was made using the relativistic relation

$$E_n = m_n c^2(\gamma - 1) = m_n c^2 \left(\frac{1}{\sqrt{1 - \left(\frac{L}{tc}\right)^2}} - 1 \right), \quad (1)$$

where $m_n = 939.6$ MeV$/c^2$ is the neutron mass, L is the neutron flight path, t is the time-of-flight of the neutron, $c = 299.8$ m/μs is the speed of light, and γ is the Lorentz factor.

In the equation the neutron time-of-flight for each event was estimated via the PSA routine relative to the γ-flash (see Sec. III A), while the neutron flight path estimation is not straightforward. The reason behind this lies in the fact that each neutron, in addition to the geometrical flight path corresponding to the distance from the edge of the spallation target (where the production of the neutron occurs) to each actinide target (where a fission event is recorded in the Micromegas detector), travels an additional distance inside the spallation target, namely the moderation length λ. The moderation length is energy dependent and corresponds to a distribution of times-of-flight which are a result of the same neutron energy, as presented in Fig. 5. Monte Carlo simulations are performed with the FLUKA code [42,43], within the n_TOF Collaboration, to describe the neutron beam produced from the spallation target. Then the neutron beam is estimated from the neutron optical transport to each actinide target, taking into account the specific characteristics of the setup.

The geometrical flight path was estimated in order to achieve the best reproduction of the ^{235}U resonances in the low energy region, by trying different flight paths for the conversion of the experimental time-of-flight to energy and by comparing them with the expected counts, calculated from the convolution of the evaluated fluence per proton pulse [24] and the reference cross section [44]. However, the correction in the energy by taking into account the mean value of the moderation length, as estimated from Fig. 5, was less than 0.7% for the entire energy range. As a result, the correction for the moderation length was negligible for this measurement. The flight path lengths used for the conversion of the time-of-flight to energy were 183.40 m for the ^{235}U target and ranged from 183.42 to 183.51 m for the ^{230}Th targets, with the difference between them being equal to their geometrical distance.

C. Correction for the lost fission fragments

One experimental effect which needs to be reliably quantified in the data analysis is related to the pulse amplitude cut applied to the data. As seen in Fig. 6 in the low neutron energy region, signals of α particles, originating from the natural radioactivity of the actinide targets, were present in the amplitude spectrum. With increasing neutron energies the contribution from the α signals decreases, while noise appears, originating from the γ-flash residuals, which increases with the neutron energy. In order to discard the α-particle and noise signals, an energy dependent amplitude cut was implemented, which defines the minimum amplitude a signal must have in order to be considered as a fission fragment. The application of this cut also removes the low-amplitude signals from fission fragments.

To estimate the fraction of the lost fission fragments, Monte Carlo simulations of the detection setup were performed with the FLUKA code [42,43]. The fission fragment atomic and mass numbers and their kinetic energy were generated using the GEF code [45]. The fission fragments were randomly generated in an actinide sample, while isotropic emission was assumed. An equivalent thickness for each target was adjusted in order to adequately reproduce the low energy region of the simulated spectra, since, even though the quantity of the actinides in the

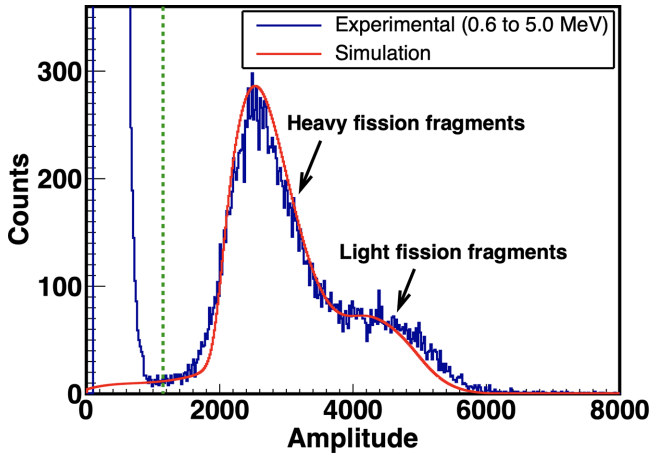

FIG. 7. Comparison between experimental (blue line) and simulated (red line) spectra (normalized in the counts of fission fragments) for one of the ^{230}Th (#3) targets, after the calibration and application of a skewed Gaussian response function to the simulated one. The amplitude cut for this energy region is presented with the dashed green line.

targets was known with high accuracy, the exact composition of the targets was not precisely known [46]. The simulated deposited energy in a Micromegas detector was convoluted with a skewed Gaussian response function, in order to reproduce the general shape of the experimental amplitude spectra.

The comparison between the experimental spectrum and the simulated for one ^{230}Th target is shown in Fig. 7 for a neutron energy range of 0.6–5.0 MeV in which no γ-flash residuals were present. The reproduction of the experimental spectrum corresponding to fission fragments is satisfactory, which ensures that the correction for the fission fragments below the applied amplitude cut is reliable. It is important to note that the ^{230}Th and the reference ^{235}U amplitude spectra exhibited similar shapes and thicknesses, which minimizes the uncertainty due to a systematic effect of this particular correction.

In order to reject the noise introduced in the amplitude spectra with the increase of the neutron energy (see Fig. 6), a higher amplitude cut was adopted in the analysis at higher energies. As the amplitude spectrum of fission fragments does not (significantly) change with neutron energy, the estimation of the lost fission fragments with this higher amplitude cut was made by comparing the spectra with high and low amplitude cuts, respectively. Then a correction factor was estimated from the ratio of an integrated region of the spectrum with the lower amplitude cut to the corresponding one with the higher cut. The region was chosen in order to obtain clean amplitude spectra for fission with both amplitude cuts. This correction is valid, since the shapes of the amplitude spectra for fission were invariant in the above mentioned energy regions.

The systematic uncertainty due to this correction was estimated to be less than 2.2% for all ^{230}Th targets. It was derived from comparing the mean cross-section value from the seven ^{230}Th targets when the amplitude cut was calculated by the FLUKA simulations and when the same amplitude cut was applied to all the targets (the seven ^{230}Th and the reference ^{235}U). The similarity in the thickness and the amplitude spectra of the ^{230}Th targets and the reference ^{235}U one results in this small deviation of the cross section results, when applying different methods for estimating the correction for the fission pulses lost due to the amplitude cut introduced in the analysis.

The simulations performed with the FLUKA code were additionally used for the estimation of the fission fragments which are emitted from the actinide target but do not manage to enter the detector gas, being absorbed inside the target. This is a result of a combination of the energy of the fission fragment and its emission angle. The correction varies and depends on the thickness of the sample: it is about 6.2% for the ^{238}U target and less than 2% for the rest of the targets. The uncertainty of this correction is included in the uncertainty due to a systematic effect of the amplitude cut correction, since the same thickness was assumed for all the targets in order to compare the absolute cross-section results of each ^{230}Th target when implementing the Monte Carlo simulations for the amplitude cut and self-absorption corrections and when a simplified approach is used, as described in Sec. III C.

D. Pileup correction

Pileup of the pulses is caused when two or more sequential pulses are recorded within a short time interval and are identified by the PSA routine as one single pulse. To consider this effect, the correction of the nonparalyzable model, as described in Ref. [47], was implemented in this analysis. When the behavior of the detector is considered to be nonparalyzable, pulses which arrive during the dead time of the detector are lost and have no effect in the response of the detector.

However, the Micromegas detector does not explicitly follow the nonparalyzable detector hypothesis, so the first step before applying the correction is to treat the detector pulses to follow the nonparalyzable model. In order to do so, when pulses appear closer in time than the fixed dead time τ, assumed to be equal to the FWHM of the pulses, the first pulse is stored, while the subsequent pulses which arrive during the dead time are discarded from the analysis. So, following the nonparalyzable case, the true interaction rate n in the detector is given by the following equation:

$$n = \frac{m}{1 - m\tau}, \tag{2}$$

where m is the recorded counting rate. It is important to note that this correction was applied independently for the dedicated and the parasitic pulse modes, which are the two pulse types available at n_TOF: the dedicated ones correspond to the nominal intensity of the proton bunch, while the parasitic ones correspond to a low intensity (approximately half of the nominal value).

It is interesting to mention that the instantaneous counting rate of the reference ^{235}U and the ^{230}Th targets was less than $\approx$ 600 kHz at all neutron energies (even for the dedicated pulse mode), exhibiting a similar dependence on neutron energy, as presented in Fig. 8. The dead time correction was less than 6.5% for the ^{230}Th and ^{235}U targets and less than 12% for the ^{238}U target. The systematic uncertainty due to pileup is considered negligible ($<$1%), since the correction was small

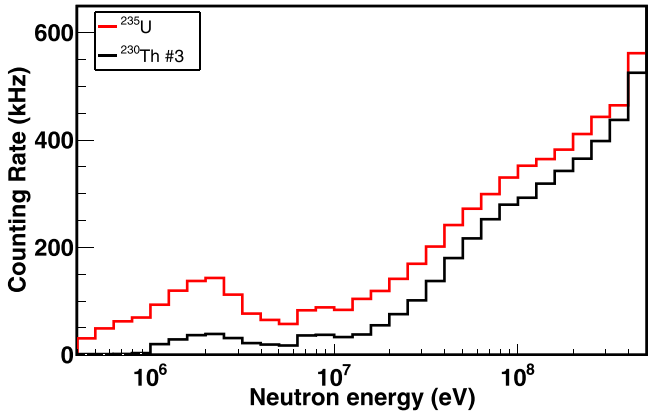

FIG. 8. Counting rate of the reference ^{235}U target (red line) and for one of the ^{230}Th targets (black line), corresponding to the dedicated pulses.

for the ^{230}Th targets and the reference ^{235}U target and at the same time a very similar behavior in the shape of the counting rate of these targets was observed.

E. Contaminants

Pu contaminants were present in the ^{230}Th samples; however, their contribution is negligible for energies higher than the fission threshold. This can be seen in Fig. 9 where the expected counts per proton for ^{230}Th are plotted in comparison with the expected counts from all the Pu isotopes in the same target. The contribution from the ^{232}Th(n, f) reaction was calculated from the amount of ^{232}Th (see Sec. II A), taking into account the neutron flux from the reference ^{235}U sample and the cross section of the reaction. The cross-section values were estimated from ENDF/B-VIII.0 [19] for energies up to 60 MeV, from the experimental values of Shcherbakov *et al.* [48] in the energy range 60 to 200 MeV, and from the point of Goldanskii *et al.* [49] at 380 MeV to cover the energy range 200 to 400 MeV, using linear interpolation to estimate the cross section in the energies of interest.

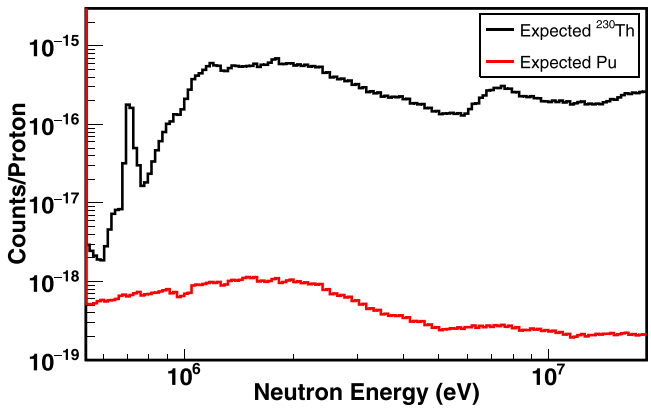

FIG. 9. Expected counts per proton for ^{230}Th (black line) and for all the Pu isotopes present in the ^{230}Th target (red line) for the experimental area EAR-1 measurement. The yield of all Pu contaminants is negligible when compared to the yield of ^{230}Th in this energy region.

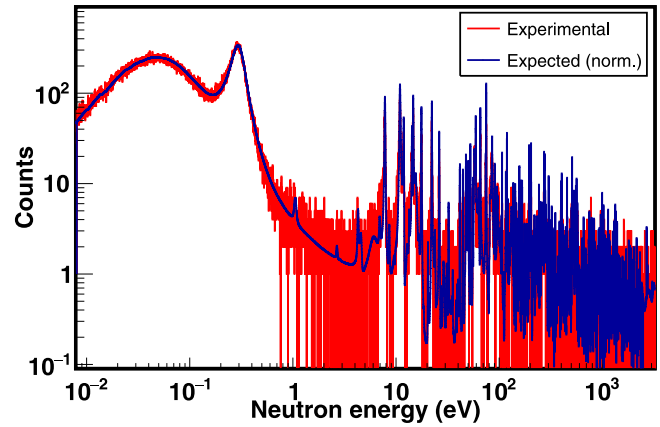

FIG. 10. Comparison between experimental counts (red line) and expected counts from the Pu contaminants present in the ^{230}Th samples (blue line) of the experimental area EAR-2 measurement. The expected counts are normalized to the experimental ones in the energy region between 4 eV and 3 keV.

The higher neutron fluence per proton pulse of the experimental area EAR-2 was exploited in order to investigate whether counts from the ^{230}Th(n, f) reaction were present on top of the Pu counts below the fission threshold. To this end, the expected counts from all the Pu isotopes present in the ^{230}Th samples were estimated, taking into account the cross section of each Pu isotope [19] and the previously evaluated neutron fluence of experimental area EAR-2 [50]. The expected counts from the Pu isotopes were compared to the experimental counts from the EAR-2 measurement, after normalization in the energy region 4 eV to 3 keV, as presented in Fig. 10. The counts from the Pu isotopes were dominant in the shown region and all the observed resonances can be attributed to the Pu isotopes. In addition, the derived thermal cross section is consistent with the expectation from the Pu isotopes.

F. Neutron scattering

Monte Carlo simulations were performed with the MCNP5 code [51] to estimate the effect of neutron scattering in the whole experimental setup. The simulated geometry consisted of the fission chamber, the Micromegas detectors, and the actinide targets with the target holders. The neutron source was described as a monodirectional disk source with a histogram of energies and a diameter equal to that of the fission collimator of EAR-1. The results of the simulations revealed negligible contributions from neutron scattering, since the difference in the neutron fluence between the targets was less than 1% for all neutron energies of interest and the uncertainty due to a systematic effect of this correction is considered negligible.

IV. RESULTS

The cross section for the ^{230}Th(n, f) reaction as a function of the incident neutron energy was derived using ^{235}U as reference (labeled "ref") by assuming a thin-sample approximation

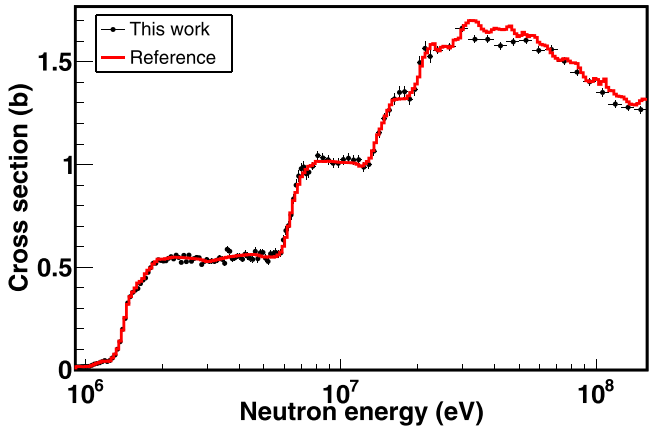

FIG. 11. Cross section of the ^{238}U(n, f) reaction (black circle), estimated using the ^{235}U(n, f) reaction as reference, plotted along with the reference cross section of ^{238}U(n, f) [19,44].

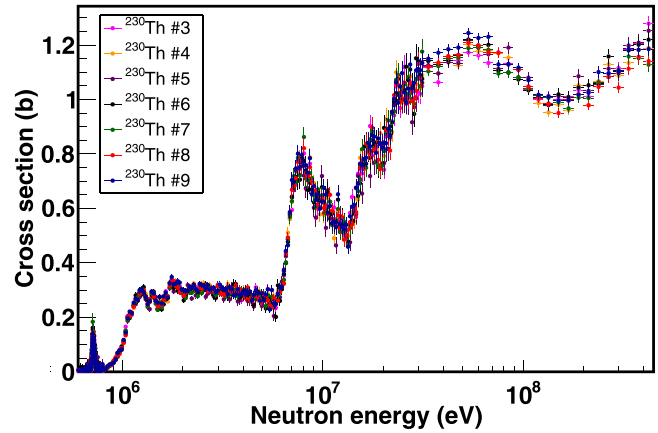

FIG. 12. Cross section from the seven ^{230}Th samples for the ^{230}Th(n, f) reaction, estimated using the ^{235}U(n, f) reaction as reference. Only the statistical errors are shown in the figure.

such that the observed count rate is directly proportional to the cross section, according to the equation

$$\sigma(E) = \frac{C(E)}{C^{\text{ref}}(E)} \times \frac{f_{\text{abs}}}{f_{\text{abs}}^{\text{ref}}} \times \frac{f_{\text{amp}}(E)}{f_{\text{amp}}^{\text{ref}}(E)} \times \frac{f_{\text{dt}}(E)}{f_{\text{dt}}^{\text{ref}}(E)} \times \frac{f_{\text{cont}}(E)}{f_{\text{cont}}^{\text{ref}}(E)} \times f_{\text{fluence}}(E) \times \frac{N}{N^{\text{ref}}} \times \sigma^{\text{ref}}(E), \quad (3)$$

where C are the counts per energy bin and pulse, f_{abs} is the correction factor for the fission fragments which do not succeed in entering the Micromegas gas, f_{amp} is the correction factor for the amplitude cut introduced in the analysis, f_{dt} is the correction factor for the dead time, f_{cont} is the correction factor for the contribution of the contaminants, and f_{fluence} is the correction factor for the difference in the fluence per proton pulse between the target and the reference sample. The total number of atoms per sample is denoted by N. To derive the number of atoms from the activities the half-lives of Ref. [30] were used: $T_{1/2} = 7.538(30) \times 10^4, 7.038(5) \times 10^8$, and $4.468(5) \times 10^9$ a for ^{230}Th, ^{235}U, and ^{238}U, respectively. Since the ^{230}Th and ^{235}U samples were prepared under identical conditions, the effective area defined by the intersection of the incident neutron beam and sample layer cancels out. In practice, this assumption is only valid if both the sample layer thickness and incident neutron beam flux do not show a spatial dependence. To account for the combined effect of a spatial dependence of the sample deposit and beam intensity an additional systematic uncertainty of 3.5% was considered. This uncertainty was estimated from the spread of the final results between the ^{230}Th samples.

A. Reproduction of the ^{238}U(n, f) cross section

For the validation of the analysis procedure described in Sec. III, the cross section of the ^{238}U(n, f) reaction was estimated using as reference the ^{235}U(n, f) one. The results are presented in Fig. 11, along with the reference cross section, taken from ENDF/B-VIII.0 [19] for energies between 0.15 and 30 MeV and from the IAEA 2017 Neutron Data Standards library for energies between 30 and 160 MeV [44].

As shown in the figure, an excellent reproduction of the reference ^{238}U(n, f) cross section is achieved from the data of this work up to 30 MeV. In the energy range between 30 and 50 MeV the cross section from the present work is lower than the reference one, with the difference being less than 5% for all neutron energies. At higher energies, namely up to 160 MeV, the agreement between the results obtained in this work and those of the reference library is very good. The deviations observed at energies higher than 30 MeV, as well as the fact that energies higher than 160 MeV could not be reached, can be solely attributed to the nature of the ^{238}U target. During the experimental campaign it was observed that a lower voltage in the mesh electrode had to be applied to the ^{238}U target, with respect to the ^{230}Th and ^{235}U targets, in order to avoid saturation of the γ-flash peak. This decrease in the gain of the Micromegas detector resulted in lower amplitude pulses, which made the analysis procedure demanding, especially in the high energy region, where the effects of the γ-flash residuals are present. Consequently, it was decided to implement the ^{238}U target only for the validation of the analysis procedure. The ^{230}Th(n, f) cross section was determined using the ^{235}U target as a reference, taking advantage of the similarity in the amplitude spectra between the targets and the comparable behavior of the pileup of the pulses (see Sec. III D) and the self-absorption correction (see Sec. III C), thus minimizing the effect of the systematic uncertainties of the measurement.

B. Cross section of the ^{230}Th(n, f) reaction

The cross-section results from the seven ^{230}Th targets, estimated using the ^{235}U(n, f) reaction as reference, are shown in Fig. 12. The cross-section values from the individual targets are in very good agreement with each other, since no systematic difference is observed between them. The results for the neutron-induced fission cross section of ^{230}Th, as estimated from the weighted average of the seven ^{230}Th targets, from the fission threshold up to 400 MeV are presented in Fig. 13, along with all available datasets, while the results for the region near the 700 keV resonance are zoomed in Fig. 14. In all the figures only the statistical uncertainties are shown.

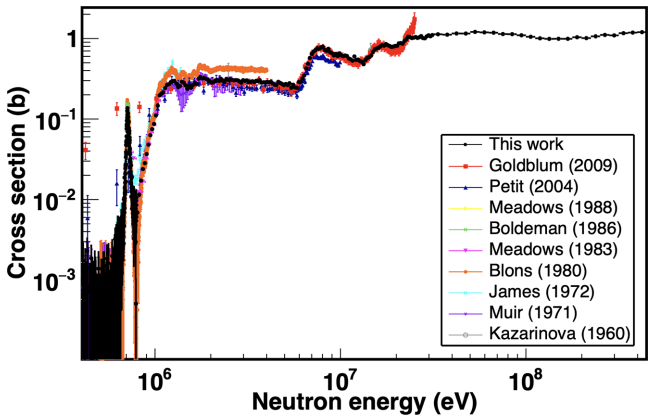

FIG. 13. Cross section of the ^{230}Th(n, f) reaction (black circle), estimated using the ^{235}U(n, f) reaction as reference, plotted along with the previous datasets. The binning is isolethargic with 2000 bins per decade (bpd) up to 0.8 MeV, 100 bpd from 0.8 to 30 MeV, and 20 bpd from 30 to 400 MeV. Only the statistical uncertainties are shown in the figure.

As seen in Fig. 14, the absolute value of the cross section in region near the 700 keV resonance from this work is lower than that of Boldeman and Walsh [11], Blons *et al.* [6], and James *et al.* [3] and higher than the data of Muir and Veeser [18]. However, it is important to note, as mentioned in the relevant publications, that the fission cross section of Blons *et al.* and James *et al.* was estimated by normalizing the fission yield per neutron to the cross-section value 0.37 b at 1.4 MeV (see Sec. I). The comparison of our data with these data sets after renormalization is shown below. The surrogate data of Goldblum *et al.* [13] and Petit *et al.* [14] do not reproduce the shape and the absolute cross section of the resonance.

Regarding the cross section at higher energies, good agreement within the uncertainties is observed between the data of the present work and the data of Meadows [15,16] and Muir and Veeser, the data point of Kazarinova *et al.* at 14.6 MeV, as

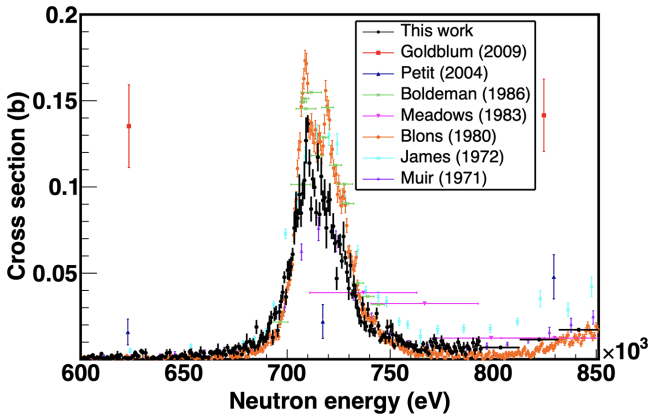

FIG. 14. Cross section of the ^{230}Th(n, f) reaction (black circle), estimated using the ^{235}U(n, f) reaction as reference, plotted along with the previous datasets in the region of the resonance near 700 keV. The binning used is isolethargic with 2000 bins per decade (bpd). Only the statistical uncertainties are shown in the figure.

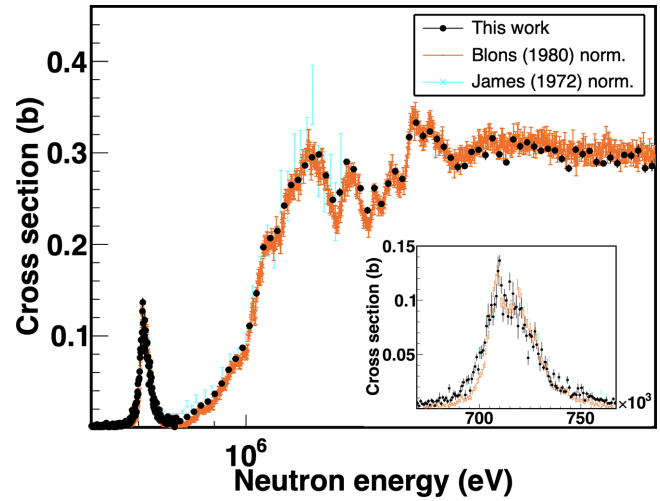

FIG. 15. Cross section of the ^{230}Th(n, f) reaction (black circle), estimated using the ^{235}U(n, f) reaction as reference, plotted along with the data of Blons *et al.* (orange points) and James *et al.* (cyan cross) normalized to the current data. Only the statistical uncertainties are shown in the figure.

well as with the data of Goldblum *et al.* for energies between 1.2 and 17 MeV, where an unphysical increase in the cross-section values in the data is observed, resulting in increasing the deviations from the present work. This deviation can be an indication of the energy limit up to which the indirect surrogate method can give reliable results for this nucleus. In addition, this comparison gives valuable information for the improvement of the relevant theoretical models which are necessary for the surrogate method, which is extremely useful in cases of nuclei inaccessible with direct measurements. Good agreement within uncertainties is also observed between this work and the data of Petit *et al.* for energies between 1 and 2.3 MeV, while at higher energies, the data of Petit *et al.* are systematically lower. Finally, the data of Blons *et al.* and James *et al.* are systematically higher than the data of the present work. Also, the data point of Kazarinova *et al.* at 2.5 MeV is above the data of this work. It is important to note that for neutron energies above 25 MeV there are no data available in the literature.

In Fig. 15 the cross-section data of the present work are presented along with the renormalized data of Blons *et al.* and James *et al.*, reducing the cross-section values by approximately 27%. As seen in the figure, when applying this renormalization a good agreement is reached among these data sets and the present work, both in the region of the resonance near 700 keV and at higher energies. This is an important observation, since the data of Blons *et al.* have the highest resolution existing in the literature. Taking this into account our data tend to confirm the structures observed in the resonance, but with somewhat lower cross-section values.

C. Uncertainties

The uncertainty due to counting statistics of the final cross section, which is the weighted average of the seven ^{230}Th

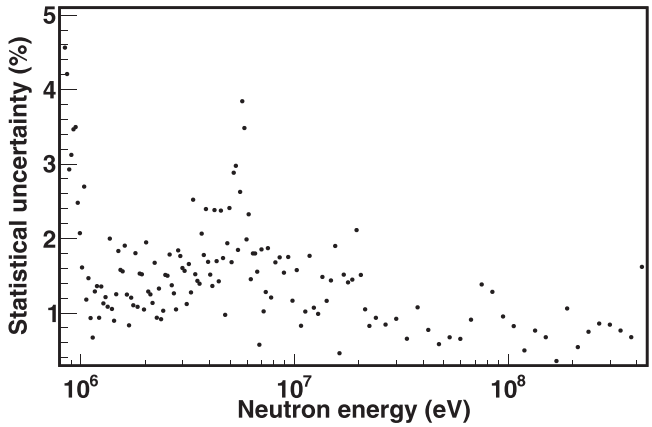

FIG. 16. Uncertainty due to counting statistics of the ^{230}Th(n, f) cross section, for energies higher than 0.8 MeV.

targets, is presented in Fig. 16 for energies higher than 0.8 MeV. It is less than 5% for all neutron energies higher than 0.8 MeV. Concerning the lower energy region, the uncertainty due to counting statistics was found to be less than ≈7% near the resonance maximum, increasing at the edges.

The systematic uncertainties of the measurement are presented in Table II. The uncertainty of the sample mass is a result of the target characterization process and is estimated to be ≈1%. The uncertainty due to the inhomogeneities of the sample deposit and the profile of the neutron beam is 3.5%, calculated from the differences observed in the ^{230}Th samples (see Sec. IV). The combined uncertainty of the amplitude cut and the self-absorption, the dead time, and the beam fluence are estimated from the analysis procedure to be <2.2%, <1%, and <1% respectively. It is important to stress here that the cross section of the ^{230}Th(n, f) reaction is calculated relative to the ^{235}U(n, f) one, with ^{230}Th values exhibiting a similar behavior to the above mentioned corrections with the reference ^{235}U target, thus minimizing the contribution of these correction factors. Finally, the uncertainty of the cross section of the reference reaction contributes to the final systematic uncertainty. This uncertainty is energy dependent and it is estimated from ENDF/B-VIII.0 [19] for energies 0.5 to 30 MeV with an uncertainty ranging from 1.2% to 1.8%, from the IAEA 2017 Neutron Data Standards library [44] for energies between 30 and 200 MeV with uncertainty between 2.2% and 4.8%, and for energies higher than 200 MeV from the IAEA Report [52] with an uncertainty ranging between 2.1% and 7.1%.

TABLE II. Systematic uncertainties of the ^{230}Th(n, f) cross-section measurement.

Contribution	Uncertainty
Sample mass	≈1%
Spatial dependence and beam intensity	≈3.5%
Amplitude cut and self-absorption correction	<2.2%
Dead time	<1%
Neutron beam fluence	<1%

V. THEORETICAL CALCULATIONS

Theoretical calculations of the ^{230}Th(n, f) reaction cross section were performed with the EMPIRE statistical model code version 3.2.3 (Malta) [53] for incident neutron energy up to 200 MeV, in an attempt to reproduce the gross structure of the experimental cross-section values obtained from this work. Beyond 200 MeV the validity of the nuclear reaction models contained in EMPIRE is no longer guaranteed; therefore, the calculation of the ^{230}Th(n, f) cross section from 200 to 400 MeV has been extended by means of an intranuclear cascade model coupled to an evaporation-fission model.

A. EMPIRE calculations

EMPIRE is a modular system of nuclear reaction codes, containing various nuclear models, and designed for calculations starting above the resonance region, in the case where the incident particle is a neutron, up to about 200 MeV.

The theoretical calculations of this work were performed within the framework of the Hauser-Feshbach model with the EMPIRE code version 3.2.3 (Malta), by assuming a double-humped fission barrier. For the calculation the decay channels with charged particles were neglected, so in addition to fission $(n$,el), $(n$,inl), (n, γ), and (n, xn) channels were taken into account. The optical model parameters were taken from the Reference Input Parameter Library (RIPL-3) [54] for the inelastic (direct) channel and for the inverse neutron channel, implementing the optical model potential of Capote *et al.* (RIPL catalog number 2408) [55]. For the preequilibrium mechanism the phenomenological model PCROSS (with a default parameter equal to 1.5) [56,57] was adopted. The modeling of the γ-ray strength functions was achieved by the modified Lorentzian MLO1 model [58], and the enhanced generalized superfluid model (EGSM) [59] was adopted to describe the level densities in the continuum of the normal states, as well as to describe the level densities for the deformations at the saddle points.

The EMPIRE calculations with the default parameters described above are presented in Fig. 17 (blue line) for the fission channel, along with the experimental cross section of this work; as shown in the figure a significant disagreement is visible. The slope and the value of the subthreshold fission is underestimated in the calculations, as are as the first-, second-, and third-chance fission, the fission plateaus, and the multi-chance fission cross sections at energies up to 75 MeV. At higher energies the cross section is generally overestimated by the EMPIRE calculation.

To improve the agreement between the EMPIRE calculations and the experimental cross-section data of this work, adjustments were made in the fission barrier heights and widths, as well as the level density parameters $\tilde{a}$ (ATILNO) of the thorium isotopes. The second fission barrier height of ^{231}Th was reduced by 8% and the width by 28%, while the first fission barrier height of the same isotope was reduced by 3%. These adjustments improved the description of the slope, as well as the values of the fission cross section up to 1.5 MeV. In addition, the level density parameter $\tilde{a}$ of ^{230}Th was increased by 25% to decrease the cross section in the

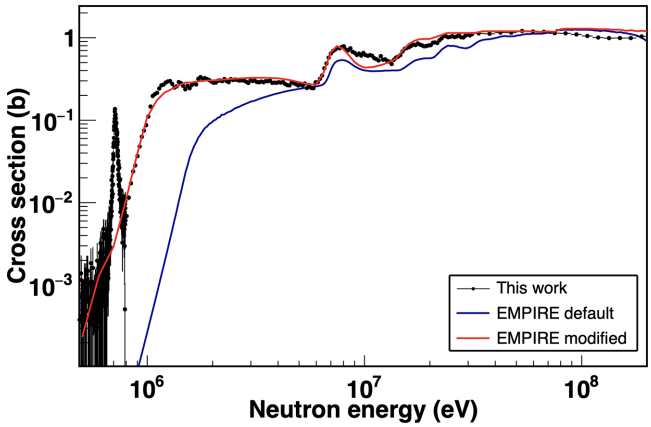

FIG. 17. EMPIRE calculation for the ^{230}Th neutron induced fission cross section (up to 200 MeV) with the default parameters (blue line) and the modified parameters (red line) along with the experimental cross section of this work (black points).

in the first-chance fission plateau between 1.5 and 6 MeV. Furthermore, by decreasing the second fission barrier height of ^{230}Th by 6% the first-chance fission cross section was better described, failing, however, to reproduce the shape and value of the cross section in the energy region from 8.5 to 13 MeV. No fission barriers exist in the RIPL-3 library, for the thorium isotopes with mass numbers lower than $A = 230$, so the fission barrier heights and widths for these isotopes were arbitrarily chosen in order to reproduce the fission cross section at higher energies. The fission barrier heights and widths of all thorium isotopes implemented in the modified calculations are presented in Table III. Finally, in order to decrease the cross section for energies higher than 10 MeV the level density parameter $\tilde{a}$ of ^{229}Th was decreased by 17%. The modified EMPIRE calculation is presented with the red line in Fig. 17.

The calculations with the modified parameters reasonably reproduce the experimental fission cross section with the exception of the resonance structure near 700 keV, the fine structures at ≈1–2 MeV, and the range ≈8–13 MeV. Additionally, at energies greater than 75 MeV, the cross-section values are overestimated. It should be mentioned that the results for the (n,inl) and (n, γ) reaction cross sections have been slightly affected by these parameter modifications, while the (n,el) and (n,tot) ones were practically unaffected.

TABLE III. Fission barrier heights (V) and widths ($\hbar\omega$) implemented in the modified EMPIRE calculation for all thorium isotopes. The values modified from the RIPL-3 default ones are presented in bold, while in italics the values are the values for the isotopes which do not exist at RIPL-3 and are adopted for the calculations.

	First barrier		Second barrier	
Isotope	V_A (MeV)	$\hbar\omega_A$ (MeV)	V_B (MeV)	$\hbar\omega_B$ (MeV)
^{223}Th	*6.00*	*0.90*	*6.70*	*0.60*
^{224}Th	*6.60*	*0.90*	*7.30*	*0.60*
^{225}Th	*6.60*	*0.90*	*7.30*	*0.60*
^{226}Th	*6.60*	*0.90*	*7.30*	*0.60*
^{227}Th	*6.60*	*0.90*	*7.30*	*0.60*
^{228}Th	*6.10*	*0.90*	*6.80*	*0.60*
^{229}Th	*6.10*	*0.90*	*6.30*	*0.60*
^{230}Th	6.10	0.90	**6.37**	0.60
^{231}Th	**5.80**	0.70	**6.15**	**0.36**

Calculations using the triple-humped fission barrier could in principle improve the cross section reproduction of the structures observed near the fission threshold; however, this lies beyond the scope of this paper, since there is still an ongoing theoretical investigation of these issues. As an example, the calculations of Sin *et al.* [60] on the ^{232}Th and ^{231}Pa nuclei, carried out with a model incorporating the triple-humped fission barriers, were able to reproduce the resonant structure in the first-chance neutron-induced fission cross sections.

The theoretical calculations of this work highlights the need for new experimental measurements in order to constrain the theoretical models and improve the calculations. The fine structures in the fission cross section of thorium isotopes, known as the thorium anomaly, have not yet been explained theoretically. Experimental measurements of the angular distributions of fission fragments, as well as of the competing channels to fission and determination of various parameters related to fission can assist in the study and the better understanding of the fission process.

B. INCL++/ABLA07 calculations

For incident neutron energy beyond 200 MeV the fission of ^{230}Th was described by Monte Carlo simulations. The 2010 IAEA benchmark of spallation models [61] recognized the Liége intranuclear cascade model INCL++, with main author Cugnon (see Ref. [62] and references therein) as one of the best spallation models when combined with the Darmstadt deexcitation model ABLA07 [63] (main author Schmidt).

Fission induced by high-energy nucleons is usually described in Monte Carlo simulations as a three-stage process: first, the incident nucleon interacts with individual nucleons in the target nucleus, producing a series of binary collisions that lead to the emission of fast nucleons, γ's, pions, and light clusters, depending on the incident energy, the so-called fast cascade. Then, the spallation remnant undergoes a preequilibrium process that brings it to a thermal equilibrium condition, eventually followed by particle evaporation, fission, or other decay modes.

The INCL++ model skips the preequilibrium stage thanks to the self-consistent calculation of the stopping time of the cascade, which marks the beginning of the equilibrium stage of the remnant, allowed to decay by the coupling with the ABLA07 model through particle evaporation, emission of light clusters, fission, or—from a prescribed excitation energy per nucleon—multifragmentation.

The ABLA07 approach to fission contains elements of dynamics, since the time evolution of the fission degree of freedom is treated as a diffusion process, determined by the interaction of collective degrees of freedom with a heat bath formed by the individual nucleons. The process is described by a Fokker-Planck equation approximately solved in

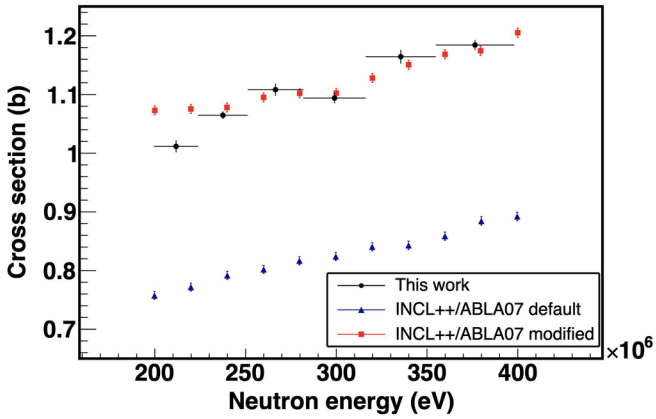

FIG. 18. Comparison of Monte Carlo calculated fission cross sections with experimental data.

analytical form. At low excitation energy the code uses a standard two-humped fission barrier, whose penetrability is computed in the approximation of full damping of the vibrational resonances in the intermediate well. The nuclear level densities at the ground state deformation and at the saddle points of the fission barrier are described by a constant temperature formula at low excitation energy and a Bethe-like formula at high energy: the latter is characterized by level density parameters α_n at the ground state deformation and α_f at the saddle point deformation.

In the present work version 5.2 of INCL++ is used [64], which is expected to work up to an incident nucleon energy of the order of 15 GeV and was already used in Ref. [65] in an attempt to extend to 1 GeV the (n, f) cross sections of some fission standards experimentally known up to 200 MeV. Following the recommendation of the authors, no change is applied in the parameters of the INCL++ code. Therefore, the possible changes for a better agreement with experimental data are limited to ABLA07, where the fission calculations are particularly sensitive to the fission barrier heights, B_f, of the equilibrated remnants, as well as to the level density parameters, α_f, at the saddle points.

The comparison of the experimental cross section points obtained from this work along with the INCL++/ABLA07 calculations with default model parameters and adjusted parameters in the incident energy range from 200 to 400 MeV is presented in Fig. 18. The default calculation strongly underestimates the experimental points, while the best fit is obtained by decreasing the fission barrier heights, B_f, of the remnants in all Monte Carlo runs by a constant amount, $\Delta B_f = -0.5$ MeV. The reduction is considerable, but note that the fission barrier heights of many remnants are unknown, or poorly determined. The fit is refined by increasing the level density parameters α_f of all remnants by a factor of 1.025. Only the experimental point at about 212 MeV is overestimated, but this might be explained by the proximity to the lower energy limit of validity of the intranuclear cascade calculations. A better fit to the experimental points in the incident energy range from 189 to 238 MeV could by obtained by reducing the enhancement factor of the level density

VI. CONCLUSIONS

The ^{230}Th(n, f) cross section has been measured with high accuracy at the neutron time-of-flight facility n_TOF at CERN with Micromegas detectors up to 400 MeV, providing the first data for neutron energies above 25 MeV. The ^{235}U(n, f) cross section was used as a reference.

The analysis procedure, including the various corrections in the recorded signals, along with Monte Carlo simulations for the amplitude spectra of the fission fragments and the neutron scattering, has been presented. The derived cross section is in a very good agreement with several experimental datasets available in literature and provides useful information to resolve previously existing discrepancies.

In addition, theoretical calculations were conducted for the ^{230}Th(n, f) reaction, which highlighted the need for new experimental data on competing reactions, which would allow constraining the parameters involved in theoretical models. These new experimental data, combined with additional measurements on fission observables, such as the angular distributions of fission fragments, can assist in the theoretical study of the fission process and the evolution of the existing theoretical models.

ACKNOWLEDGMENTS

This project received funding from the Euratom "Support safe operation of nuclear systems" program 2014–2018 under Grant Agreement No. 847552 (SANDA) and by the funding agencies of the participating institutes. This research is implemented through the IKY scholarships program and cofinanced by the European Union (European Social Fund 'ESF) and Greek national funds through the action entitled "Reinforcement of Postdoctoral Researchers - 2nd call (MIS 5033021)", in the framework of the Operational Programme "Human Resources Development Program, Education and Lifelong Learning" of the National Strategic Reference Framework.

[1] D. Greneche and M. Chhor, in *Development of the Thorium Fuel Cycle* (Woodhead, Cambridge, UK, 2012), Chap. 8, pp. 177–202.

[2] G. Yuen, G. T. Rizzo, N. Behkami, and J. R. Huizenga, Fragment angular distributions of the neutron-induced fission of ^{230}Th, Nucl. Phys. A **171**, 614 (1971).

[3] G. D. James, J. E. Lynn, and L. G. Earwaker, Nuclear spectroscopy of highly deformed ^{230}Th, Nucl. Phys. A **189**, 225 (1972).

[4] M. Mirea, L. Tassan-Got, C. Stephan, C. O. Bacri, and R. C. Bobulescu, Fine structure of the 0.7 MeV resonance in the ^{230}Th neutron-induced fission cross-section, Europhys. Lett. **73**, 705 (2006).

[5] J. Blons, C. Mazur, D. Paya, M. Ribrag, and H. Weigmann, Rotational Bands in Asymmetrically Deformed ^{230}Th, Phys. Rev. Lett. **41**, 1282 (1978).

[6] J. Blons, C. Mazur, D. Paya, M. Ribrag, and H. Weigmann in Proceedings of the 18th International Winter Meeting on Nuclear Physics, Bormio, 1980 (unpublished).

[7] J. W. Boldeman, D. Gogny, A. R. de L. Musgrove, and R. L. Walsh, Fission fragment angular distributions for neutron fission of ^{230}Th, Phys. Rev. C **22**, 627 (1980).

[8] J. E. Lynn, The concept of vibrational resonances associated with the secondary and tertiary wells of a multi-humped fission barrier, J. Phys. G: Nucl. Phys. **9**, 665 (1983).

[9] J. Blons, C. Mazur, D. Paya, M. Ribrag, and H. Weigmann, On the existence of triple-humped fission barriers in ^{231,233}Th, Nucl. Phys. A **414**, 1 (1984).

[10] J. E. Lynn, Fission-fragment angular distributions for ^{230}Th(n, f) in the vicinity of the 715 keV resonance, Nucl. Phys. A **445**, 37 (1985).

[11] J. W. Boldeman and R. L. Walsh, Neutron fission of thorium-230 revisited, Radiat. Eff. **92**, 317 (1986).

[12] P. Möller and J. R. Nix, Calculation of fission barriers, in *Physics and Chemistry of Fission, Proceedings of the third IAEA Symposium*, Rochester, 13–17 August 1973, STI/PUB/347 Vol. 1 (IAEA, Vienna, 1974), pp. 103–143.

[13] B. L. Goldblum, S. R. Stroberg, J. M. Allmond, C. Angell, L. A. Bernstein, D. L. Bleuel, J. T. Burke, J. Gibelin, L. Phair, N. D. Scielzo, E. Swanberg, M. Wiedeking, and E. B. Norman, Indirect determination of the ^{230}Th(n, f) and ^{231}Th(n, f) cross sections for thorium-based nuclear energy systems, Phys. Rev. C **80**, 044610 (2009).

[14] M. Petit, M. Aiche, G. Barreau, S. Boyer, N. Carjan, S. Czajkowski, D. Dassié, C. Grosjean, A. Guiral, B. Haas *et al.*, Determination of the ^{233}Pa(n, f) reaction cross section from 0.5 to 10 MeV neutron energy using the transfer reaction ^{232}Th(^{3}He,p)^{234}Pa, Nucl. Phys. A **735**, 345 (2004).

[15] J. W. Meadows, The fission cross sections of ^{230}Th, ^{232}Th, ^{233}U, ^{234}U, ^{236}U, ^{238}U, ^{237}Np, ^{239}Pu and ^{242}Pu relative to ^{235}U at 14.74 MeV neutron energy, Ann. Nucl. Energy **15**, 421 (1988).

[16] J. W. Meadows, The fission cross sections of some thorium, uranium, neptunium and plutonium isotopes relative to ^{235}U, Argonne National Laboratory Technical Report No. ANL/NDM-83 (Argonne National Laboratory, Argonne, Illinois, 1983).

[17] M. I. Kazarinova, Y. S. Zamyatnin, and V. M. Gorbachev, Fission cross sections for Th^{230}, Pu^{240}, Pu^{241}, and Am^{241} by neutrons with energies of 2.5 and 14.6 MeV, Sov. J. At. Energy **8**, 125 (1961).

[18] D. W. Muir and L. R. Veeser, Neutron-induced fission cross sections of ^{230}Th and ^{231}Pa (1971) in Proceedings of the Third International Conference on Neutron Cross Sections and Technology, Knoxville, 1971 (unpublished), p. 292.

[19] D. A. Brown, M. B. Chadwick, R. Capote, A. C. Kahler, A. Trkov, M. Herman, A. Sonzogni, Y. Danon, A. Carlson, M. Dunn *et al.*, ENDF/B-VIII.0: The 8th major release of the Nuclear Reaction Data Library with CIELO-project cross sections, new standards and thermal scattering data, Nucl. Data Sheets **148**, 1 (2018).

[20] K. Shibata, O. Iwamoto, T. Nakagawa, N. Iwamoto, A. Ichihara, S. Kunieda, S. Chiba, K. Furutaka, N. Otuka, T. Ohsawa *et al.*, JENDL-4.0: A new library for nuclear science and engineering, J. Nucl. Sci. Technol. **48**, 1 (2011).

[21] A. Plompen, O. Cabellos, C. D. S. Jean, M. Fleming, A. Algora, M. Angelone, P. Archier, E. Bauge, O. Bersillon, R. Blokhin *et al.*, The joint evaluated fission and fusion nuclear data library, JEFF-3.3, Eur. Phys. J. A **56**, 1 (2020).

[22] A. J. Koning, D. Rochman, J.-C. Sublet, N. Dzysiuk, M. Fleming, and S. van der Marck, TENDL: Complete nuclear data library for innovative nuclear science and technology, Nucl. Data Sheets **155**, 1 (2019).

[23] C. Guerrero, A. Tsinganis, E. Berthoumieux, M. Barbagallo, F. Belloni, F. Gunsing, C. Weiss, E. Chiaveri, M. Calviani, V. Vlachoudis *et al.*, Performance of the neutron time-of-flight facility n_TOF at CERN, Eur. Phys. J. A **49**, 1 (2013).

[24] M. Barbagallo, C. Guerrero, A. Tsinganis, D. Tarrío, S. Altstadt, S. Andriamonje, J. Andrzejewski, L. Audouin, V. Bécares, F. Becvar *et al.*, High-accuracy determination of the neutron flux at n_TOF, Eur. Phys. J. A **49**, 156 (2013).

[25] C. Weiß, E. Chiaveri, S. Girod, V. Vlachoudis, O. Aberle, S. Barros, I. Bergström, E. Berthoumieux, M. Calviani, C. Guerrero *et al.* (n_TOF Collaboration), The new vertical neutron beam line at the CERN n_TOF facility design and outlook on the performance, Nucl. Instrum. Methods Phys. Res., Sect. A **799**, 90 (2015).

[26] G. Sibbens, A. Gook, D. Lewis, A. Moens, S. Oberstedt, D. Vanleeuw, R. Wynants, and M. Zampella, Target preparation for neutron-induced reaction experiments, EPJ Web Conf. **229**, 04003 (2020).

[27] Z. Varga and G. Surányi, Production date determination of uranium-oxide materials by inductively coupled plasma mass spectrometry, Analytica Chimica Acta **599**, 16 (2007).

[28] C. Venchiarutti, R. Jakopič, C. Hennessy, and K. Toth, Preparation and characterisation of uranium and plutonium quality control samples for isotope dilution mass spectrometry measurements and uncertainty estimation, J. Radioanal. Nucl. Chem. **327**, 1305 (2021).

[29] J. Heyse, M. Anastasiou, R. Eykens, A. Moens, A. Plompen, P. Schillebeeckx, G. Sibbens, D. Vanleeuw, and R. Wynants, Characterization of ^{235}U targets for the development of a secondary neutron fluence standard, J. Radioanal. Nucl. Chem. **299**, 1055 (2014).

[30] A. Nichols, D. Aldama, and M. Verpelli, Handbook of nuclear data for safeguards: Database extensions, IAEA Report No. INDC(NDS)-0534 (IAEA Nuclear Data Section,Vienna, Austria, 2008).

[31] S. Pommé, L. Johansson, G. Sibbens, and B. Denecke, An algorithm for the solid angle calculation applied in alpha-particle counting, Nucl. Instrum. Methods Phys. Res., Sect. A **505**, 286 (2003).

[32] K. Luyckx, Karakterisatie van fissiele en fertiele splijtlagen voor nauwkeurige neutronenmetingen, M.S. thesis, XIOS Hogeschool Limburg, 2008 (unpublished).

[33] R. Capote, S. Badikiv, A. Carlson, I. Duran, F. Gunsing, D. Neudecker, V. Pronyaev, P. Schillebeecxk, G. Schnabel, D. Smith, and A. Wallner, Unrecognized sources of uncertainties

(USU) in experimental nuclear data, Nucl. Data Sheets **163**, 191 (2020).
[34] S. Richter, *Standardization of JRC Developed Nuclear Mass Spectrometry Methods with ASTM-International* (Publications Office of the European Union, Luxembourg, 2016).
[35] D. Vanleeuw, J. Heyse, G. Sibbens, and M. Zampella, Preparation and characterization of ^{10}B targets at JRC-Geel, EPJ Web Conf. **229**, 03005 (2020).
[36] L. Shekhtman, Micropattern gaseous detectors, Nucl. Instrum. Methods Phys. Res., Sect. A **494**, 128 (2002).
[37] Y. Giomataris, Development and prospects of the new gaseous detector "Micromegas", Nucl. Instrum. Methods Phys. Res., Sect. A **419**, 239 (1998).
[38] S. Andriamonje, D. Attie, E. Berthoumieux, M. Calviani, P. Colas, T. Dafni, G. Fanourakis, E. Ferrer-Ribas, J. Galan, T. Geralis *et al.*, Development and performance of Microbulk Micromegas detectors, J. Instrum. **5**, P02001 (2010).
[39] S. Andriamonje, M. Calviani, Y. Kadi, R. Losito, V. Vlachoudis, E. Berthoumieux, F. Gunsing, A. Giganon, Y. Giomataris, C. Guerrero *et al.*, A transparent detector for n_TOF neutron beam monitoring, J. Korean Phys. Soc. **59**, 1597 (2011).
[40] P. Žugec, C. Weiß, C. Guerrero, F. Gunsing, V. Vlachoudis, M. Sabate-Gilarte, A. Stamatopoulos, T. Wright, J. Lerendegui-Marco, F. Mingrone *et al.* (n_TOF Collaboration), Pulse processing routines for neutron time-of-flight data, Nucl. Instrum. Methods Phys. Res., Sect. A **812**, 134 (2016).
[41] A. Stamatopoulos, A. Tsinganis, N. Colonna, M. Kokkoris, R. Vlastou, M. Diakaki, P. Žugec, P. Schillebeeckx, F. Gunsing, M. Sabaté-Gilarte *et al.* (n_TOF Collaboration), Investigation of the ^{240}Pu(n, f) reaction at the n_TOF/EAR2 facility in the 9 meV–6 MeV range, Phys. Rev. C **102**, 014616 (2020).
[42] T. T. Böhlen, F. Cerutti, M. P. W. Chin, A. Fassò, A. Ferrari, P. Ortega, A. Mairani, P. Sala, G. Smirnov, and V. Vlachoudis, The FLUKA code: developments and challenges for high energy and medical applications, Nucl. Data Sheets **120**, 211 (2014).
[43] G. Battistoni, F. Cerutti, A. Fassò, A. Ferrari, S. Muraro, J. Ranft, S. Roesler, and P. R. Sala, The FLUKA code: description and benchmarking, AIP Conf. Proc. **896**, 31 (2007).
[44] A. D. Carlson, V. G. Pronyaev, R. Capote, G. M. Hale, Z.-P. Chen, I. Duran, F.-J. Hambsch, S. Kunieda, W. Mannhart, B. Marcinkevicius *et al.*, Evaluation of the neutron data standards, Nucl. Data Sheets **148**, 143 (2018).
[45] K.-H. Schmidt, B. Jurado, C. Amouroux, and C. Schmitt, General description of fission observables: GEF model code, Nucl. Data Sheets **131**, 107 (2016).
[46] G. Sibbens, M. Ernstberger, T. Gouder, M. Marouli, A. Moens, A. Seibert, D. Vanleeuw, M. Zúñiga, T. Wiss, M. Zampella, and E. Zuleger, Morphological and compositional study of ^{238}U thin film targets for nuclear experiments, AIP Conf. Proc. **1962**, 030007 (2018).
[47] G. F. Knoll, *Radiation Detection and Measurement* (Wiley, New York, 1989).
[48] O. Shcherbakov, A. Donets, A. Evdokimov, A. Fomichev, T. Fukahori, A. Hasegawa, A. Laptev, V. Maslov, G. Petrov, S. Soloviev, Y. Tuboltsev, and A. Vorobyev, Neutron-induced fission of ^{233}U, ^{238}U, ^{232}Th, ^{239}Pu, ^{237}Np, ^{nat}Pb and ^{209}Bi relative to ^{235}U in the energy range 1–200 MeV, J. Nucl. Sci. Technol. **39**, 230 (2002).
[49] V. I. Goldanskii, V. S. Penkina, and E. Tarumov, Fission of heavy nuclei by high energy neutrons, J. Exp. Theor. Phys. **2**, 677 (1956).
[50] M. Sabaté-Gilarte, M. Barbagallo, N. Colonna, F. Gunsing, P. Žugec, V. Vlachoudis, A. Stamatopoulos, J. Lerendegui-Marco, M. Cortés-Giraldo, A. Villacorta *et al.*, High-accuracy determination of the neutron flux in the new experimental area n_TOF-EAR2 at CERN, Eur. Phys. J. A **53**, 210 (2017).
[51] X.-. M. C. Team, MCNP, A General Monte Carlo N-Particle Transport Code, Version 5, Los Alamos National Laboratory Report No. LA-UR-03-1987, 2005 (unpublished).
[52] B. Marcinkevicius, S. Simakov, and V. Pronyaev, ^{209}Bi(n, f) and ^{nat}Pb (n,f) Cross Sections as a New Reference and Extension of the ^{235}U, ^{238}U and ^{239}Pu(n, f) Standards up to 1 GeV, IAEA Report No. INDC(NDS)0681 (IAEA Nuclear Data Section, Vienna, Austria, 2015).
[53] M. Herman, R. Capote, B. V. Carlson, P. Obložinský, M. Sin, A. Trkov, H. Wienke, and V. Zerkin, EMPIRE: Nuclear reaction model code system for data evaluation, Nucl. Data Sheets **108**, 2655 (2007).
[54] R. Capote, M. Herman, P. Obložinský, P. G. Young, S. Goriely, T. Belgya, A. V. Ignatyuk, A. J. Koning, S. Hilaire, V. A. Plujko *et al.*, RIPL - Reference input parameter library for calculation of nuclear reactions and nuclear data evaluations, Nucl. Data Sheets **110**, 3107 (2009).
[55] R. Capote, E. Soukhovitskii, J. M. Quesada, and S. Chiba, *Lane Consistency of the Dispersive Coupled-Channel Optical Model Potential* (EDP Sciences, Les Ulis, France, 2008), p. 239.
[56] J. J. Griffin, Statistical Model of Intermediate Structure, Phys. Rev. Lett. **17**, 478 (1966).
[57] C. K. Cline, The Pauli exclusion principle in pre-equilibrium decay, Nucl. Phys. A **195**, 353 (1972).
[58] V. A. Plujko, A new closed-form thermodynamic approach for radiative strength functions, Acta Phys. Pol. B **31**, 435 (2000).
[59] A. D'Arrigo, G. Giardina, M. Herman, A. V. Ignatyuk, and A. Taccone, Semi-empirical determination of the shell correction temperature and spin dependence by means of nuclear fission, J. Phys. G: Nucl. Part. Phys. **20**, 365 (1994).
[60] M. Sin, R. Capote, A. Ventura, M. Herman, and P. Obložinský, Fission of light actinides: ^{232}Th(n, f) and ^{231}Pa(n, f) reactions, Phys. Rev. C **74**, 014608 (2006).
[61] S. Leray, J. C. David, M. Khandaker, G. Mank, A. Mengoni, N. Otsuka, D. Filges, F. Gallmeier, A. Konobeyev, and R. Michel, Results from the IAEA benchmark of spallation models, J. Korean Phys. Soc. **59**, 791 (2011).
[62] J. Hirtz, J.-C. David, A. Boudard, J. Cugnon, S. Leray, I. Leya, J. L. Rodríguez-Sánchez, and G. Schnabel, Strangeness production in the new version of the Liège intranuclear cascade model, Phys. Rev. C **101**, 014608 (2020).
[63] A. Kelič, M. V. Ricciardi, and K.-H. Schmidt, ABLA07—Towards a complete description of the decay channels of a nuclear system from spontaneous fission to multifragmentation, IAEA Report No. INDC(NDS)0530 (IAEA Nuclear Data Section, Vienna, Austria, 2008).
[64] D. Mancusi, A. Boudard, J. Cugnon, J.-C. David, P. Kaitaniemi, and S. Leray, Extension of the Liège intranuclear-cascade model to reactions induced by light nuclei, Phys. Rev. C **90**, 054602 (2014).
[65] I. Duran, A. Ventura, S. L. Meo, D. Tarrío, L. Tassan-Got, and C. Paradela, On the search for a (n,f) cross-section reference at intermediate energies, EPJ Web Conf. **146**, 02032 (2017).

Correction: The previously published Figure 18 contained incorrect entries in the legend and has been replaced.